# On the feasibility of a temperature state observer for powder bed fusion additive manufacturing

Nathaniel Wood, David J. Hoelzle, Member

Abstract—Powder bed fusion (PBF) is the additive manufacturing (AM) process that has arguably the highest potential for the elevation of AM from rapid prototyping tools to the use in the manufacture of final products. The initial success of PBF has been in spite of the primary mechanism material addition, directed energy by a laser or electron beam, being controlled in open-loop using detailed process maps and heuristics. This manuscript details an exploratory study of one enabling control tool in the system of tools required for closed-loop control of directed energy: state-observation for the estimation of temperature states throughout the part from measurements of surface temperatures. We pose the fundamental physics of PBF with the variational calculus of the finite element method (FEM), and then repose FEM as a state-space model. From the state-space model, we define a temperature state observer and corresponding observability criteria. The significant outcomes of this study are the first definition of a state observer for PBF temperature fields and the successful estimation of the temperature evolution of several simulated test parts.

#### I. INTRODUCTION

Additive Manufacturing (AM) tools are a diverse set of computer controlled manufacturing systems that selectively add materials in a layer-by-layer fashion [1]; often described as freeform, this manufacturing mode enables the fabrication of complex features such as internal channels [2] and interconnected porosity [3]. Of the set of AM tools, the class termed powder bed fusion (PBF) AM [1] has received particular attention from industry for their ability to meet or exceed wrought mechanical properties using established engineering materials, for example metal alloys such as Ti-6Al-4V [4] and Inconel 718 [5]. PBF tools (Fig. 1a), such as selective laser sintering, direct metal laser sintering, and electron beam melting, build three-dimensional parts using a build cycle of: 1) spread a thin layer (20 - 100  $\mu$ m) of powdered feedstock, 2) selectively melt a two-dimensional pattern using a high-powered laser or electron beam, and 3) index the build platform in the negative z direction to prepare for the next layer. Unlike many traditional thermal material forming processes such as casting, in which the liquid to solid transformation occurs approximately globally and simultaneously [6], the directed energy to melt the material is local, where the melt pool surrounding the laser

Final manuscript submitted on February 23, 2018. This work was supported in part by start-up funds from the Ohio State University. The authors acknowledge technical support from ANSYS.

Nathaniel Wood is with the Department of Mechanical and Aerospace Engineering at the Ohio State University, Columbus, OH, 43210 USA (email: wood.863@osu.edu).

David J. Hoelzle is with the Department of Mechanical and Aerospace Engineering at the Ohio State University, Columbus, OH, 43210 USA (phone: +1 (614) 688-2942; email: hoelzle.1@osu.edu).

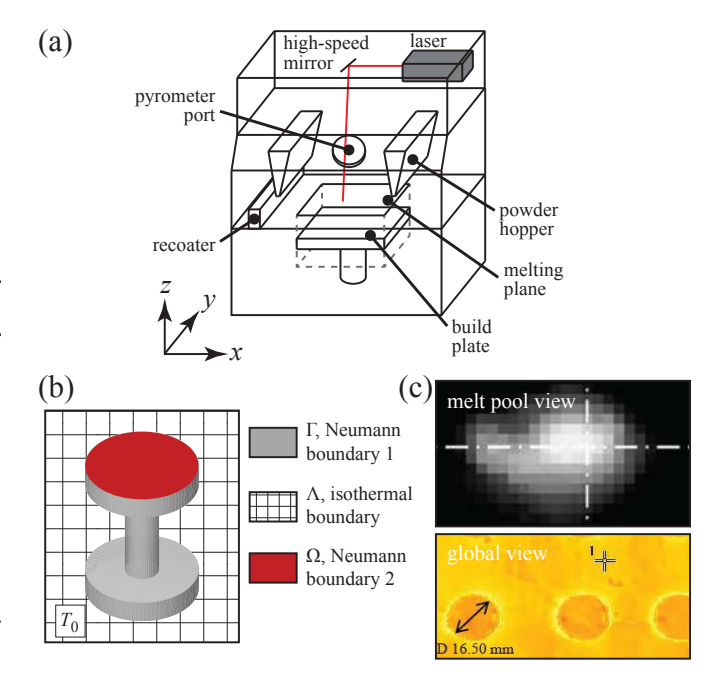


Fig. 1. **Powder bed fusion (PBF) additive manufacturing.** (a) System schematic demonstrating key components of PBF. (b) Assumed boundary conditions for the temperature model, Eqn. (2), used here. (c) There are two common temperature measurement modes: global melting plane temperature measurement (image sourced from [13]) and local melt pool temperature measurement (image sourced from [14]).

or electron beam is on the order of 1 mm [7], [8]. Consequently, temperature gradients are extremely large, exceeding 500 K/mm for metal parts [9], [10], yielding differential thermal contraction and local thermal micro-distortions that can integrate to yield large, millimeter scale distortions [11], [12]

Despite PBF itself being a sophisticated, computer-controlled tool, material deposition feedback is simplistic; most commercial PBF systems use an open-loop melt-pool temperature regulation scheme [15]. While the potential benefits of closed-loop surface temperature regulation are obvious, the main technical limitation preventing closed-loop control is inadequate sensing [16]. Temperature sensing must be remote as a thermocouple cannot be placed on the surface being built. Most commercial systems have a thermocouple built in to the build plate for chamber temperature regulation, but the temperature at the melting plane is hundreds of degrees Kelvin higher than at the build plate. Some research-grade PBF tools and some commercial systems, such as the Concept Laser M2, monitor the melt pool using a digital camera based pyrometer with an optical path that is con-

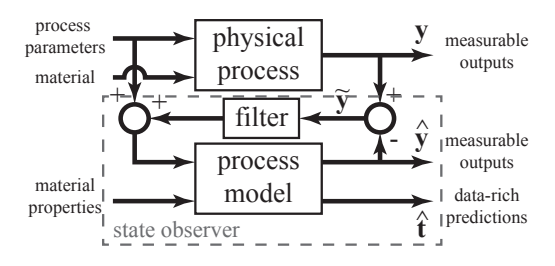


Fig. 2. **Idea of a temperature observer for PBF.** The main purpose of the temperature observer is to better estimate actual internal temperatures during manufacturing.

centric with the laser beam using sophisticated optics [17], [18] (Fig. 1c melt pool view). Other commercial systems and a multitude of research PBF tools have used global-view digital camera based pyrometers to thermally image the top surface [15], [19], [20] (Fig. 1c global view). Regardless of temperature sensing mode, thermal sensing is remote and, at present, there are no ways to measure temperature past the top layer being built; the sensing limitation is simple, fused metal is opaque to infrared transmission.

If we had the ability to estimate the temperature history of the entire part during a build, we would have the ability to employ a cadre of process validation and quality control tools. For instance, process faults could be detected by measuring the difference between estimated temperature states and predicted temperature states. Temperature history directly influences metallurgic phase formation [21], that thus influences mechanical properties and corrosion resistance; a complete temperature history would enable us to predict phases composition at all locations in a part. Temperature history influences the melt pool size [22]; an accurate estimate of the sub-surface temperatures could be integrated into a feedback control system designed to modulate laser power.

To this end, this manuscript explores the feasibility of applying the standard idea of a state observer to estimate the temperature of underlying layers of material. State-observers are a common control systems tool that merges a model running along side real-time measurements to estimate unmeasured process states, filter measured signals, or states without a physical interpretation, for the purposes of control. However, the PBF process is very different from the standard state-observer problem: the physical system to observe has spatiotemporal dynamics, the size of the system, or number of states, is continually increasing as more material is added, and both the addressed input channels - location of heat input - and addressed output channels - location of sensed temperatures – are continually changing with laser or e-beam spot location and layer, respectively. Work has been done on constructing state observers to control melt pool dynamics [23], whereas this manuscript focuses on state observers that model the temperature history of the entire part.

This work is a first, exploratory look at the feasibility of state-observation for the PBF process (Fig. 2). The spatiotemporal thermal model is developed in Section II, where we make assumptions that simplify the continually

growing model described in the previous paragraph. This model sets up the idea of a temperature state-observer for PBF; we explore observability criteria in Section III. The paper concludes with a simple PBF simulation study in Sections IV and V and concluding remarks in Section VI.

Throughout this paper, we will use notation that is common to the controls community, as opposed to the standard for the FEM community. Scalars will be denoted by regular letters, vectors will be denoted by lower-case bold letters (e.g. v), and matrices denoted by upper-case bold letters (e.g. A).

# II. SPATIOTEMPORAL THERMAL MODEL

# A. Definition of Fourier's Law for PBF

Consider the problem of a heat source,  $q(\mathbf{v},t)$ , impinging on a solid material at spatial location  $\mathbf{v} = \{x,y,z\} \in V$ ,  $V \subseteq \mathbb{R}^3$ , and time  $t \in \mathbb{R}_+$ . The material temperature,  $T(\mathbf{v},t)$ , is defined by the heat flux balance

$$C\frac{\partial T}{\partial t} = q - q_{\text{cond.}} - q_{\text{conv.}} - q_{\text{rad.}}$$
 (1)

where heat is transferred by conduction,  $q_{\rm cond.}$ , convection,  $q_{\rm conv.}$ , and radiation,  $q_{\rm rad.}$ , and C is the capacitance of the material. This standard heat flux balance is employed by many PBF temperature prediction packages employing finite element method (FEM) based solvers, ranging in complexity from detailed models of the melt pool mechanics to simplified models for whole part simulation. For the purposes of a model that can be run alongside an actual experiment, we will employ common simplifying assumptions.

- **A1.** The Biot number for PBF is approximately Bi = 0.01, thus  $q_{\text{conv.}} = 0$  and  $q_{\text{rad.}} = 0$  [24].
- **A2.** Conduction into the unfused powder is negligible as the loosely packed powder is a poor conductor [25]. This sets up the insulated Neumann boundary condition at the part periphery,  $\nabla T \cdot \hat{\mathbf{n}} = 0 \ \forall \ \mathbf{v} \in \Gamma$ , where  $\nabla = \left(\frac{\partial}{\partial x}, \frac{\partial}{\partial y}, \frac{\partial}{\partial z}\right)$ ,  $\cdot$  is the vector dot product,  $\Gamma$  is the periphery and top domain and  $\hat{\mathbf{n}}$  is the direction normal to the domain  $\Gamma$  (Fig. 1b, Neumann boundary 1).
- **A3.** The bottom surface, domain  $\Lambda$ , is isothermal with temperature  $T_0$ , setting up the Dirichlet boundary condition  $T = T_0 \ \forall \ \mathbf{v} \in \Lambda$  and t (Fig. 1b, Dirichlet boundary).
- **A4.** The top surface of a given layer,  $\bar{\mathbf{v}} = \{x, y, \bar{z}\}$ , has a prescribed thermal flux  $q(\bar{\mathbf{v}}, t)$  from the incident radiant laser/e-beam source. Similarly, only the temperature of the top surface can be observed by a thermal sensor,  $y = T(\bar{\mathbf{v}}, t)$ .
- **A5.** The last, and perhaps most tenuous, assumption is that the top layer is composed of fully-fused metal with an equivalent thermal conductivity to the bulk. Of course this is not true in the actual process, but this assumption effectively fixes the boundary conditions and retains a constant model domain.

These assumptions set up the standard partial differential equation defined by Fourier's Law

$$\frac{\partial T}{\partial t} = \frac{K}{c\rho} \nabla^2 T + \frac{q}{c\rho}$$

$$T = T_0 \ \forall \ \mathbf{v} \in \Lambda$$

$$\nabla T \cdot \hat{\mathbf{n}} = 0 \ \forall \ \mathbf{v} \in \Gamma$$
(2)

where K is the thermal conductivity of the material, c the specific heat, and  $\rho$  the material density. The arbitrarily shaped, thus complex, boundary conditions enabled by PBF and arbitrary heat flux equation q, in general, assures that there is not a closed-form solution to (2). As is common in the PBF research community, a FEM solution is sought. The FEM solution will leverage the functional, or weak, form of (2)

$$\pi = \int_{V} \left( \frac{1}{2} (\nabla T)^{T} \kappa \nabla T - QT + \rho c \dot{T} T \right) dV$$

$$- \int_{\Gamma} (q_{B} T) d\Gamma$$
(3)

where  $\kappa \in \mathbb{R}^{3 \times 3}$  is an array that contains directional heat conductivity properties, and  $q_B$  specifies the heat flux on the boundary [26]. To help with reader intuition, the first integrand captures intra-volume heat transfer, generation, and storage, and the second integrand inter-volume heat transfer.

# B. FEM model

The FEM permits a computational solution to a near infinite variety of part geometries, boundary conditions, and load conditions. This sub-section is meant to be a brief introduction to the FEM; those interested in a complete description of FEM theory and practice should consult [27].

The FEM heat transfer problem consists of five main steps:

- 1) Specify the system geometry and material properties.
- Discretize the system geometry into a collection of elements, defined by the associated nodes at their vertices, and specify the boundary and loading conditions of the system.
- 3) Construct a set of linear algebraic equations that approximate the temperature distribution within each element, based on the element boundary conditions and loads on the element.
- 4) Assemble these elemental equation systems into a global system of equations, and solve for the temperature at all nodes.
- 5) Interpolate the temperature distribution within each element by using the temperatures of its bounding nodes, which approximates the continuous temperature distribution of the system.

The elemental algebraic equations of Step 3 are derived from solving the weak form of heat transfer equation, (3). Nodal temperatures are collected in a column vector  $\mathbf{t_e}$ , and one interpolates T by the equation [26]

$$T(x, y, z) = \mathbf{n}(x, y, z)\mathbf{t_e}.$$
 (4)

n is a row vector whose elements are all functions of space that ensure that the resulting interpolated field satisfies

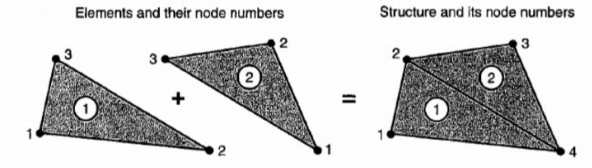


Figure 2.5-1. A hypothetical four-node structure built of two triangular three-node elements. Each node has one d.o.f.

$$[\mathbf{K}] = [\mathbf{k}]_1 + [\mathbf{k}]_2 = \begin{bmatrix} a_1 & a_3 & 0 & a_2 \\ a_7 & a_9 & 0 & a_8 \\ 0 & 0 & 0 & 0 \\ a_4 & a_6 & 0 & a_5 \end{bmatrix} + \begin{bmatrix} 0 & 0 & 0 & 0 \\ 0 & b_9 & b_8 & b_7 \\ 0 & b_6 & b_5 & b_4 \\ 0 & b_3 & b_2 & b_1 \end{bmatrix}$$

Fig. 3. Global system construction process, reproduced from [27] with permission from John Wiley and Sons, Inc.

continuity and boundary conditions. These shape functions  ${\bf n}$  are what are used in Step 5 to reconstruct the temperature field from nodal temperature values.

 $T=\mathbf{nt_e}$  is substituted into (3), and then the system potential energy is minimized by setting  $\partial \Pi/\partial \mathbf{T}=\mathbf{0}$ . This expression reduces to

$$\mathbf{K}_{\mathbf{e}}\mathbf{t}_{\mathbf{e}} + \mathbf{C}_{\mathbf{e}}\dot{\mathbf{t}}_{\mathbf{e}} = \mathbf{r}_{\mathbf{e}} \tag{5}$$

where  $K_{\rm e}$  and  $C_{\rm e}$  are scalar matrices that represent the thermal conductivity and heat capacitance of the element, and  ${\bf r_e}$  is a vector that distributes any volumetric, surface, or line loads among the nodes of the element for an optimally accurate approximation [26]. The FEM model is made ready for solution in Step 4 by assembling the elemental equations, (5), into the global equation of the form

$$\mathbf{M}\dot{\mathbf{t}} + \mathbf{K}\mathbf{t} = \mathbf{r} \tag{6}$$

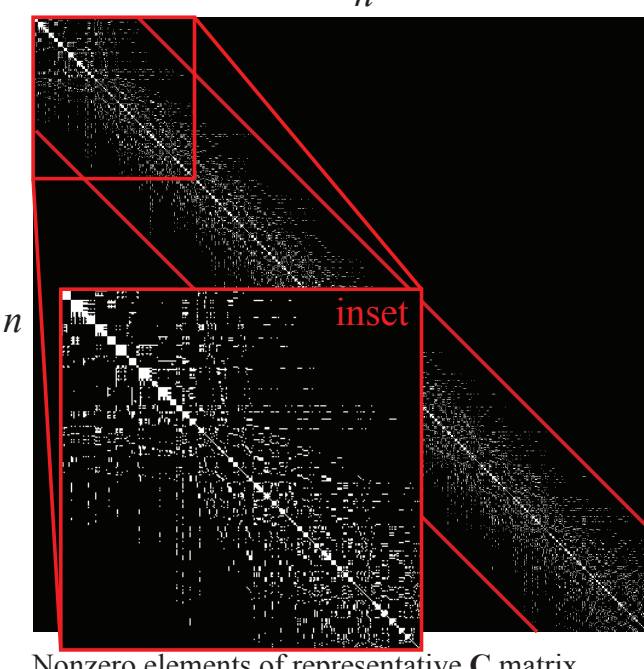
 $\dot{\mathbf{t}} \in \mathbb{R}^{n \times 1}$  is the vector containing the temperature of all n nodes in the system.  $\mathbf{M} \in \mathbb{R}^{n \times n}$ ,  $\mathbf{K} \in \mathbb{R}^{n \times n}$ , and  $\mathbf{r} \in \mathbb{R}^{n \times 1}$  are the globally-assembled counterparts of  $\mathbf{C_e}$ ,  $\mathbf{K_e}$ , and  $\mathbf{r_e}$ , respectively. After the assembly of (3), FEM software packages would solve the system of equations at each timestep specified by a variety of ODE approximation algorithms. Fig. 3 illustrates the construction of a global  $\mathbf{K}$  matrix from two elemental matrices. Note that elemental ordering is not always intuitive; optimization algorithms organize elements to minimize the band of non-zero elements in  $\mathbf{K}$  about the diagonal.

Remark 1: The Fourier heat transfer problem yields matrices  $\mathbf{M}$  and  $\mathbf{K}$  that are real-valued, symmetric, and positive-definite matrices of size  $n \times n$  [26]. Consequently,  $\mathbf{M}^{-1}$  always exists and (6) can be rearranged to isolate  $\dot{\mathbf{t}}$ ,

$$\dot{\mathbf{t}} = -\mathbf{M}^{-1}\mathbf{K}\mathbf{t} + \mathbf{M}^{-1}\mathbf{r}.\tag{7}$$

Furthermore,  $-\mathbf{M}^{-1}\mathbf{K}$  is Hurwitz by the properties of the eigenvalues of the product of symmetric, positive-definite matrices [28].

Nonzero elements of representative A matrix



Nonzero elements of representative C matrix

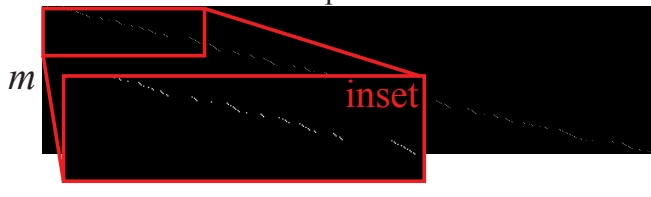


Fig. 4. Nonzero element locations of representative  $\mathbf{A} \in \mathbb{R}^{n \times n}$  and  $\mathbf{C} \in$  $\mathbb{R}^{m \times n}$  matrices. The red bars on the  $\hat{\mathbf{A}}$  matrix indicate the approximate bounds of the nonzero element band, which is 196 entries wide. Insets provide a closer view of the pattern of non-zero elements of the matrices.

## C. State-Space Representation

Equation (7) is of the standard state-space form

$$\dot{\mathbf{t}} = \mathbf{A}\mathbf{t} + \mathbf{B}\mathbf{u} \tag{8}$$

where  $A = -M^{-1}K$  and  $Bu = M^{-1}r$ . Note, that the thermal loading vector r already specifies the load to be uniformly applied to only the top-layer, Assumption 4, by construction of the global matrix from appropriately designed elemental matrices. The second part of Assumption 4, that only the top layer temperatures are measurable, is enforced by proper selection of  $\mathbf{C} \in \mathbb{R}^{m \times n}$ ,

$$y = \mathbf{Ct}. (9)$$

where there are m temperature nodes at the top surface.

A is heavily sparse, and symmetric. For ease of visualization, the A and C matrices for a typical system are shown in Fig. 4. The sparseness of Fig. 4A is due to special FEM routines which optimize the tightness of the nonzero band. Such sparseness is of critical importance when computing the dynamics of systems that contain between 1000 and 10,000 states.

#### III. OBSERVABILITY

As (8) and (9) are in the form of the standard state space equation, all textbook notions of observability can be analyzed as per usual. This section highlights useful analysis tools as they apply to the PBF system defined in Section II.

We use that standard definition of observability detailed in [29] and others: state equations (8)-(9) are "said to be observable if for any unknown initial state" t(0)", there exists a finite  $t_1 > 0$  such that knowledge of the input **u** and the output y over  $[0, t_1]$  suffices to determine uniquely the initial state" t(0). All standard checks on the observability of the pair (A, C) are valid; here we find it convenient to leverage the rank test of the observability matrix  $\mathcal{O}$ . As stated in [29], the pair (A, C) is observable if

$$\mathcal{O} = \begin{bmatrix} \mathbf{C} \\ \mathbf{C}\mathbf{A} \\ \vdots \\ \mathbf{C}\mathbf{A}^{n-1} \end{bmatrix}$$
 (10)

has full column rank n. Furthermore, for unobservable (8)– (9), the number of unobservable modes is  $n - \text{Rank}(\mathcal{O})$ .

Theorem 1: Thermal model (8)–(9) is detectable.

*Proof:* Detectability follows directly from the statement in Remark 1 that  $\mathbf{A} = -\mathbf{M}^{-1}\mathbf{K}$  is Hurwitz.

## A. Observability with disconnected structures

PBF is particularly adept as making branching structures, which often results in segments that will be disconnected at some point in the build. Fig. 5 demonstrates a partially completed build in which segments of a branched structure are disconnected at the given layer, but will become connected in a future layer. As seen in the A and C matrices, the disconnect in segments yields state equations of the form

$$\begin{bmatrix} \dot{\mathbf{t}}_{1} \\ \dot{\mathbf{t}}_{2} \end{bmatrix} = \underbrace{\begin{bmatrix} \mathbf{A}_{1} & \mathbf{0} \\ \mathbf{0} & \mathbf{A}_{2} \end{bmatrix}}_{\mathbf{A}} \begin{bmatrix} \mathbf{t}_{1} \\ \dot{\mathbf{t}}_{2} \end{bmatrix} + \underbrace{\begin{bmatrix} \mathbf{B}_{1} \\ \mathbf{0} \end{bmatrix}}_{\mathbf{B}} u$$

$$\mathbf{y} = \underbrace{\begin{bmatrix} \mathbf{C}_{1} & \mathbf{0} & \mathbf{0} \end{bmatrix}}_{\mathbf{C}} \begin{bmatrix} \mathbf{t}_{1} \\ \dot{\mathbf{t}}_{2} \end{bmatrix},$$
(11)

where the upper-right and lower-left 0 sub-matrices of A indicate that there is no heat transfer between disconnected thermal masses: states  $t_1$  and  $t_2$ . None of states corresponding to temperatures t<sub>2</sub> are measured, as indicated in Fig. 5 and the right-most 0 sub-matrix of C in (11).

Corollary 1: A thermal model (8)–(9) that can be written in the form of (11) via row-rearrangement is not observable.

Proof: Corollary 1 is proven via construction of the observability matrix,  $\mathcal{O}$ . Given  $\mathbf{A}_1 \in \mathbb{R}^{n_1 \times n_1}$  and  $\mathbf{A}_2 \in$  $\mathbb{R}^{n_2 \times n_2}$ ,  $n_1 + n_2 = n$ , observability matrix  $\mathcal{O}$  equals

$$\mathcal{O} = \begin{bmatrix} \begin{bmatrix} \mathbf{C}_1 & \mathbf{0} \\ \mathbf{C}_1 & \mathbf{0} \end{bmatrix} \mathbf{A}_1 & \mathbf{0} \\ \vdots \\ \begin{bmatrix} \mathbf{C}_1 & \mathbf{0} \end{bmatrix} \mathbf{A}_1^{n-1} & \mathbf{0} \end{bmatrix}, \tag{12}$$

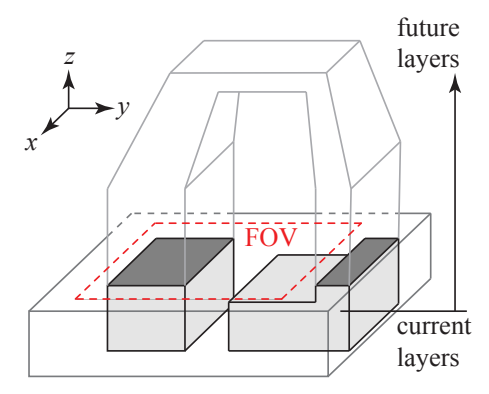


Fig. 5. **Observability of disconnected structures.** In the hypothetical scenario here, the partially-built bridged structure has two legs, one in which there are observable states and one in which the temperature measurements are either occluded by infrared opaque powder or out of the field of view (FOV).

which has a maximum column rank of  $n_1 < n$ .

# B. 'Strongly' and 'Weakly' Observable Modes

Standard observability tests for (8)–(9) (e.g. the rank rest) is of little practical importance as large scale systems (order of 10<sup>4</sup> nodes) may contain hundreds of 'weakly' observable modes in which  $\mathcal{O}$  may barely pass the rank test. Worse yet, numerical algorithms for computing matrix rank may be sensitive to a user specified tolerance, such as the Matlab rank and obsvf commands. For systems with non-defective A, we avoid these issues in detecting unobservable modes by placing the system in modal canonical form (MCF), and counting how many columns of the transformed C matrix contain no nonzero values. In MCF, each zero column of C corresponds to exactly one unobservable state, as noted in [30]. This technique cannot be repeated for systems with defective A, since numerically computing the analogous Jordan form cannot be done reliably due to the problem being ill-conditioned [31]. Additionally, we use the Hankel Singular Values (HSVs) of (8)–(9) to ascertain the relative observability of system modes. HSVs are described in [29], [32] and in many other linear systems texts, and are primarily used for performing a balanced reduction of larger systems. Here, we use the standard definition of the set of HSVs as

$$\Sigma = \operatorname{diag}\left(\sigma_1 \ge \sigma_2 \ge \ldots \ge \sigma_{n-\operatorname{Rank}(\mathcal{O})} > 0\right) \tag{13}$$

where each  $\sigma_i$  is  $\sqrt{\lambda_i(\mathbf{W}_c\mathbf{W}_o)}$ ;  $\lambda_i$  denotes the  $i^{th}$  eigenvalue of a matrix, and  $\mathbf{W}_c$  and  $\mathbf{W}_o$  are the controllability and observability grammians, respectively. From this ordered set of HSVs, an engineering decision can be made to determine how many states are 'strongly' observable and how many are 'weakly' observable; similar in spirit to [32], here we define a 'strongly' observable state as one that  $\sigma_i \geq 10^{-4}\sigma_1$  and a 'weakly' observable state as one that  $\sigma_i < 10^{-4}\sigma_1$ . Note that the count of the number of HSVs,  $n-\mathrm{rank}\,(\mathcal{O})$ , will be dependent on the tolerance of the rank test; regardless, nearly unobservable states will have a low magnitude  $\sigma_i$  and thus be 'weakly' observable.

## C. Observer design

As diagramed in Fig. 2, our aim is to design a full-state observer to estimate temperatures of nodes at positions  $0 < z < \overline{z}$ . As such, we build the standard state-observer [29]

$$\dot{\hat{\mathbf{t}}} = \mathbf{A}\hat{\mathbf{t}} + \mathbf{B}u + \mathbf{L}(\mathbf{y} - \mathbf{C}\hat{\mathbf{t}}). \tag{14}$$

A myriad of observer design algorithms can be used to design observer gain matrix **L**. We choose to use a Kalman filter design [33].

#### IV. SIMULATION SETUP

In this first exploratory study of temperature observation in PBF, we perform a simplified simulation study to help understand the basic properties of the PBF temperature observer and the effects of part geometry. The temperature output of a high-fidelity FEM simulation is used as a surrogate for an actual PBF experiment; the temperature data provides the 'true' temperatures of every node,  ${\bf t}$ . The temperature observer is built by constructing the  ${\bf A}$ ,  ${\bf B}$ , and  ${\bf C}$  matrices from a lower-fidelity FEM model, which provides temperature estimates  ${\bf \hat{t}}$  based on top-surface measurements  ${\bf y}$  taken from the lower-fidelity simulation. In brief:

- Matrices K, M, and r for the lower-fidelity observer are generated by the software ANSYS. These matrices are exported to Matlab for observer analysis and design.
   A, B, and C are constructed from K, M, and r using Eqn. (7). Additionally, top-surface measurements y were taken for the purposes of conducting the state estimation.
- 2) The high-fidelity FEM simulation in performed in AN-SYS the 'true' temperatures of every node, t.
- 3) The state estimation,  $\hat{\mathbf{t}}$ , was interpolated onto the nodes of the fine mesh. Estimation accuracy was tested by three metrics:
  - (a) Estimation error at every state:  $\tilde{\mathbf{t}} = \mathbf{t} \hat{\mathbf{t}}$ .
  - (b) Maximum error magnitude at every state:  $\mathbf{\tilde{t}}_{\max} = \max_{t} |\mathbf{\tilde{t}}(t)|$ .
  - (c) Steady-state error magnitude at every state:  $SSE(\tilde{\mathbf{t}}) = |\tilde{\mathbf{t}}(t_f)|$ , where  $t_f$  is the final time-point of the simulation.

# A. Test Parts

A set of four parts was selected to test different aspects of the PBF temperature observer. Fig. 6 supplies the geometric details of the parts used in these simulation studies. A basic block (Fig. 6a) is the simplest geometry and tests basic observer functionality. Fig. 6b and Fig. 6c represent a stress test of observability. The "spool" presents two large collections of nodes, connected by a relatively thin filament. Doing so forces the model to predict the state in the wide spool lower region, using only the small collection of neck states as a connector to the output y measured at the top surface. Fig. 6b is an unsupported spool and Fig. 6c presents the more realistic situation, in which support material joins the two ends of the spool; note that the support material has different thermal properties from the bulk material. Fig.

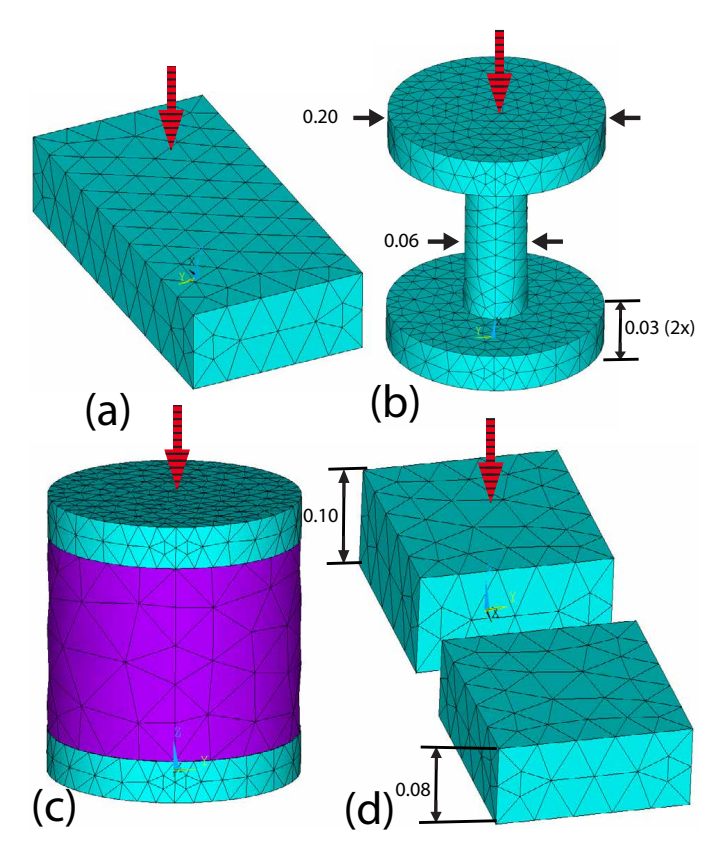


Fig. 6. **Parts used during simulation study.** Red, striped arrows indicate the surfaces subjected to heat input. All indicated dimensions are in [m] (a) 0.50m x 0.25m x 0.10m block (b) Spool without support material. (c) Spool with support material, shown in violet. Overall height of spool is 0.20m. (d) Part used to provoke failure of full state observability, as discussed in Section III-A. (d) is formed by splitting block from (a) in half and changing indicated dimensions.

TABLE I

Node count and downsampling ratios for simulation study

part	node count		downsample ratio
	coarse mesh	fine mesh	
Fig. 6a	1407	41,352	29.4
Fig. 6b	7992	49,175	6.15
Fig. 6c	9635	58,179	6.04
Fig. 6d	1363	46,310	34.0

6d tests the scenario illustrated in Section III-A. The 0.08m block of Fig. 6d contributes no measurements to the output vector and has no thermal link to the other block. Given the analysis in Section III-A, we expect all nodes of the hidden block to be unobservable. The four parts and the low-fidelity and high-fidelity node counts are tabulated in Tb. I; the spool parts required a smaller downsampling ratio to make observer analysis computationally tractable.

All test parts shared a common material. The material approximated the thermal properties of aluminum at room temperature [34]: conductivity k=250 (W/m<sup>2</sup>K), density  $\rho=2700$  (kg/m<sup>3</sup>), and specific heat c=900 (J/kgK). The support material was assumed to be comprised of air with a volume fraction of 0.45. Via Ashby's law [35], the support material effective conductivity,  $k_s$ , and density,  $\rho_s$  were

scaled by the volume fraction:  $k_s = 0.45k$  and  $\rho_s = 0.45\rho$ . These given material parameters were fed into (3), which dictated the entries of **A** and **B** by the process described in Section II.

# B. Simulated Experiment Parameters

All four tests subjected the part to the same loading conditions, designed to reflect the assumptions of Section II-A. The faces indicated by the striped red arrows in Fig. 6 were subjected to a uniform, static heat input of 100 (kW/m²). The constraints in Eqn. (2) were applied with  $T_0=294.15$  K. Interpolation was performed using three-dimensional Gaussian interpolation in the x,y, and z directions (standard deviation  $\sigma_{x,y,z}=0.0167$  m for Parts a and d and 0.005 for parts b and c) and one-dimensional Gaussian interpolation in the time direction (standard deviation  $\sigma_t=1.25$  sec for parts a and d and 2.00 sec for parts b and c).

### C. Observer Design

The Kalman filter was designed with zero-mean, white process noise w and measurement noise v with covariances  $E(ww^T)=1e5,\ E(vv^T)=1e(-6)*\mathbf{I}_m,\ \text{and}\ E(wv^T)=0,$  which were used as inputs to the MATLAB function kalman.

#### V. SIMULATION RESULTS

Table II provides the observability of the four different thermal systems corresponding to the four different parts. All four systems produced A matrices will all-distinct eigenvalues, so the observability check described in Section III-B was applied. In relation to statements on observability in Section III, the disconnected structure in Part (d) produced a larger number of unobservable states, as predicted. Part (c) had a minority of unobservable states, although it is unclear if the states are truly unobservable or if the rank test is sensitive to a tolerance. By investigating the HSVs, we can see that only about 10 % of that states for Parts b and c are strongly observable by evaluation of the HSVs.

The results of the simulation study are collated in Fig. 7 and Table II. It can be seen that the estimations of Parts (a), (c) and (d) were highly accurate. Fig. 7iiia, Fig. 7iiic and Fig. 7iiid show that the interpolated SSE for these simulations was within 5 K for the vast majority of states in the systems, and the analogous figures in row ii of Fig. 7 shows that the maximum absolute error was similarly contained. The simulation of Part (b) was less accurate, but it also represented the unrealistic scenario of the test part being manufactured without support material.

TABLE II
OBSERVABILITY AND HSV STUDY

Part	Unobservable states	% strong HSVs
Fig. 6a	0	50.1
Fig. 6b	0	11.2
Fig. 6c	3	11.7
Fig. 6d	511	26.6

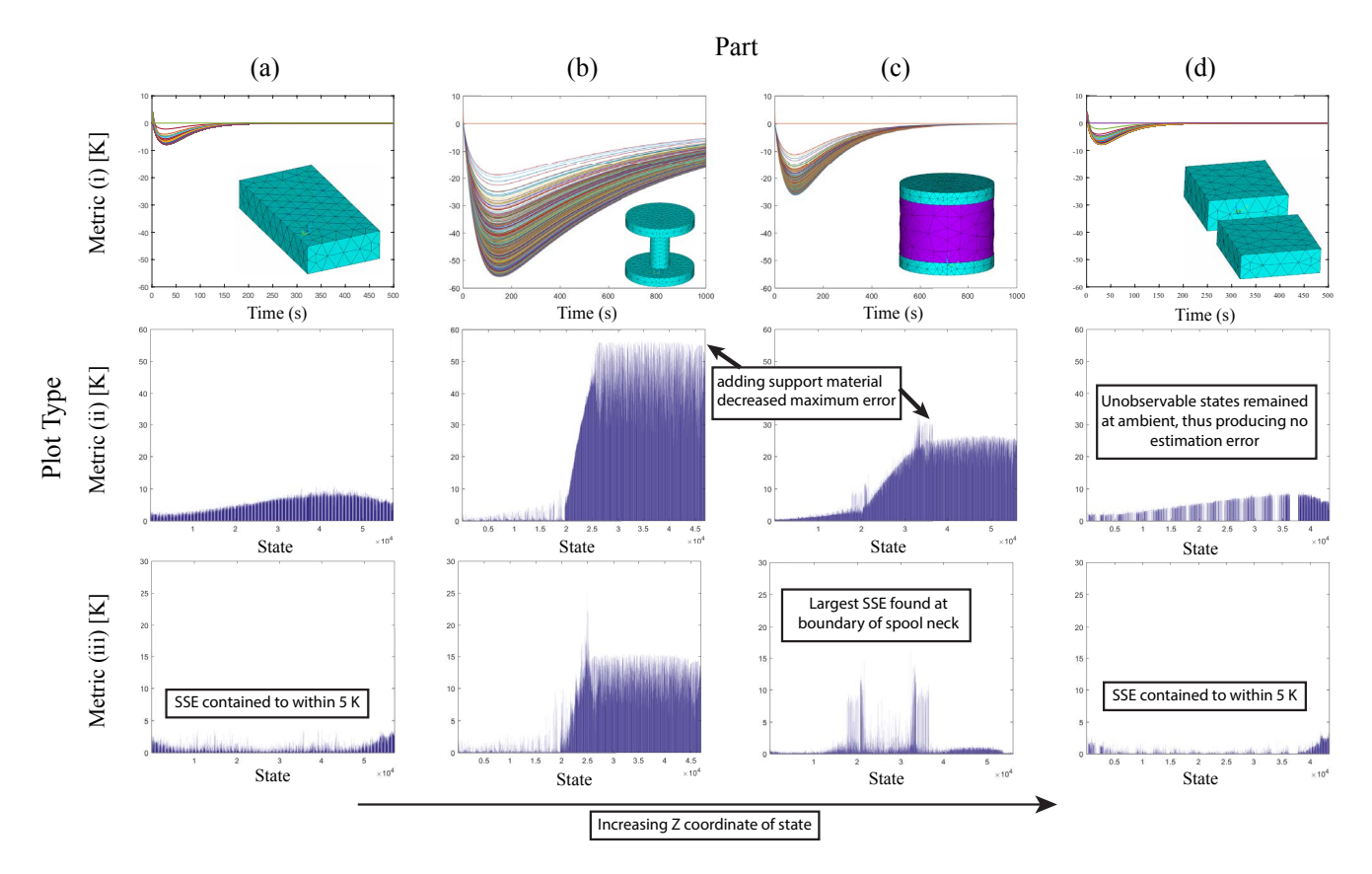


Fig. 7. Simulation study results. Grid columns (a), (b), (c), and (d) display the results corresponding to the parts as labeled in 6. Rows denote the three metrics used (Section IV): i)  $\tilde{\mathbf{t}}$ , ii)  $\tilde{\mathbf{t}}_{\max}$ , and iii) SSE  $(\tilde{\mathbf{t}})$ . State numbers are ordered from the bottom to the top of the part.

Row ii of Fig. 7 demonstrates a clear relationship between maximum absolute error and state number. Higher states showed higher error. As explained in Fig. 7, states were ordered by increasing z-coordinate. The states closest to the heat input, being those with large z-coordinates, experienced the most dramatic temperature fluctuations with time, and thus thus produced the largest error during estimation. Fig. 7iiib and Fig. 7iiic show that the largest SSE  $(\tilde{\mathbf{t}})$  occurred in the middle of the hourglass-shaped part, which corresponded to the hourglass neck.

Comparing the data in columns (b) and (c) of Fig. 7 shows that the simulation belonging to Part (c) was dramatically more accurate than that of Figure (b). The addition of the support material is the clear explanation for this result, as all other parameters of the two simulations were identical. The proportion of strong HSVs was the same for the two simulations, which eliminated the explanation used for why Part (a) and (d) were more accurate than the others. Fig. 7ib and Fig. 7ic show that the better accuracy of the Part (c) simulation was due the much more rapid convergence of the error signals with respect to those of Part (b). Simple investigation of the eigenvalues of A - LC does not explain the difference in the convergence rate of t between the two systems; future work will investigate better descriptive statistics to understand the observer convergence for largescale (order of 10<sup>4</sup> states) systems.

## VI. CONCLUSIONS

This paper is a first, exploratory work to study full state observers to estimate the temperature of defined nodal states in a PBF manufacturing. The observer is based on a Finite Element Method thermal model, which provides unconditional detectability and stability, and allows for ready construction under a vast array of part geometries and load conditions. For parts subjected to static heat flux along the top face, the observer reconstructed the temperature history at all states within the nodally-discretized part with maximum and steady-state error on the order of temperature deviation that is important to metallurgical study.

This exploratory study focused on developing the basic analysis tools to quantify observability and notions of relative observability for this application. Several simplifying assumptions were employed to define these basic tools; as we transition to a more realistic model, the weakened assumptions will yield interesting future research questions. In particular, Assumptions A4 and A5 simplified the heat source to be distributed across the top surface and the size of the model to be fixed. However, in practice, the heat input is a rastered Gaussian source and the model size is monotonically increasing as more powder, which has negligible conductivity in powder state, is fused and thus increases the thermal mass and adds new conduction pathways. We must model this time-varying and order-varying system and

define the observability of this new system. Additionally, PBF systems are often equipped with thermal cameras and can accommodate a multitude of thermocouples; thorough experiments must be performed to fully test PBF temperature observer efficacy.

#### REFERENCES

- ASTM International, "Standard terminology for Additive Manufacturing technologies, Tech. Rep. F2792-12a, 2012.
- [2] E. Sachs, E. Wylonis, S. Allen, M. Cima, and H. Guo, "Production of injection molding tooling with conformal cooling channels using the three dimensional printing process," *Polymer Engineering & Science*, vol. 40, no. 5, pp. 1232–1247, 2000.
- [3] Y. Xie, L. E. Rustom, A. M. McDermott, J. D. Boerckel, A. J. W. Johnson, A. G. Alleyne, and D. J. Hoelzle, "Net shape fabrication of calcium phosphate scaffolds with multiple material domains," *Biofabrication*, vol. 8, no. 1, p. 015005.
- [4] X. Wang, X. Gong, and K. Chou, "Scanning speed effect on mechanical properties of Ti-6Al-4V alloy processed by electron beam additive manufacturing," *Procedia Manufacturing*, vol. 1, no. Supplement C, pp. 287 295, 2015, 43rd North American Manufacturing Research Conference, NAMRC 43, 8-12 June 2015, UNC Charlotte, North Carolina. United States.
- [5] K. Amato, S. Gaytan, L. Murr, E. Martinez, P. Shindo, J. Hernandez, S. Collins, and F. Medina, "Microstructures and mechanical behavior of inconel 718 fabricated by selective laser melting," *Acta Materialia*, vol. 60, no. 5, pp. 2229 – 2239, 2012.
- [6] L. Nastac, J. Valencia, M. Tims, and F. Dax, "Advances in the Solidification of IN718 and RS5 Alloys," in *Superalloys*. TMS, 2001, pp. 103–112.
- [7] H. L. Wei, J. Mazumder, and T. DebRoy, "Evolution of solidification texture during additive manufacturing," *Scientific Reports*, vol. 5, p. 16446, Nov. 2015.
- [8] W. E. King, A. T. Anderson, R. M. Ferencz, N. E. Hodge, C. Kamath, S. A. Khairallah, and A. M. Rubenchik, "Laser powder bed fusion additive manufacturing of metals; physics, computational, and materials challenges," *Applied Physics Reviews*, vol. 2, no. 4, 2015.
- [9] K. Zeng, D. Pal, H. J. Gong, N. Patil, and B. Stucker, "Comparison of 3dsim thermal modelling of selective laser melting using new dynamic meshing method to ansys," *Materials Science and Technology*, vol. 31, no. 8, pp. 945–956, 2015.
- [10] H. Peng, D. B. Go, R. Billo, S. Gong, M. R. Shankar, B. Aboud Gatrell, J. Budzinski, P. Ostiguy, R. Attardo, C. Tomonto, J. Neidig, and D. J. Hoelzle, "Part-scale model for fast prediction of thermal distortion in dmls additive manufacturing; part 2: a quasistatic thermo-mechanical model," in *Proc. of the International Solid Freeform Fabrication Symposium*, Austin, TX, 2016.
- [11] —, "Part-scale model for fast prediction of thermal distortion in dmls additive manufacturing; part 1: a thermal circuit network model," in *Proc. of the International Solid Freeform Fabrication Symposium*, Austin, TX, 2016.
- [12] T. Krol, C. Seidel, J. Schilp, M. Hofmann, W. Gan, and M. Zaeh, "Verification of structural simulation results of metal-based additive manufacturing by means of neutron diffraction," *Physics Procedia*, vol. 41, pp. 849 – 857, 2013, lasers in Manufacturing (LiM 2013).
- [13] E. Rodriquez, F. Medina, D. Espalin, C. Terrazas, D. Muse, C. Henry, E. MacDonald, and R. B. Wicker, "Integration of a thermal imaging feedback control system in Electron Beam Melting," in *Proceedings* of the Annual International Solid Freeform Fabrication Symposium, Austin, TX, 2012, pp. 945 – 961.
- [14] M. Schmidt, F. Vollertsen, M. Geiger, S. Berumen, F. Bechmann, S. Lindner, J.-P. Kruth, and T. Craeghs, "Laser assisted net shape engineering 6, proceedings of the lane 2010, part 2 quality control of laser- and powder bed-based additive manufacturing (am) technologies," *Physics Procedia*, vol. 5, pp. 617 – 622, 2010.
- [15] G. Tapia and A. Elwany, "A review on process monitoring and control in metal-based additive manufacturing," ASME. J. Manuf. Sci. Eng., vol. 136, no. 6, 2014.
- [16] S. K. Everton, M. Hirsch, P. Stravroulakis, R. K. Leach, and A. T. Clare, "Review of in-situ process monitoring and in-situ metrology for metal additive manufacturing," *Materials & Design*, vol. 95, pp. 431 445, 2016.

- [17] J. Benda, "Temperature controlled selective laser sintering," in *Proc.* of the Annual International Solid Freeform Fabrication Symposium, Austin, TX, 1994, pp. 277–284.
- [18] S. Clijsters, T. Craeghs, S. Buls, K. Kempen, and J.-P. Kruth, "In situ quality control of the selective laser melting process using a high-speed, real-time melt pool monitoring system," *The International Journal of Advanced Manufacturing Technology*, vol. 75, no. 5, pp. 1089–1101, 2014.
- [19] B. Cheng, S. Price, J. Lydon, K. Cooper, and K. Chou, "On process temperature in powder-bed electron beam additive manufacturing: Model development and validation," ASME. J. Manuf. Sci. Eng., vol. 136, no. 6, 2014.
- [20] H. Krauss, C. Eschey, and M. Zaeh, "Thermography for monitoring the selective laser melting process," in *Proc. of the International Solid Freeform Fabrication Symposium*, Austin, TX, 2012.
- [21] M. M. Kirka, K. A. Unocic, N. Raghavan, F. Medina, R. R. Dehoff, and S. S. Babu, "Microstructure development in electron beam-melted inconel 718 and associated tensile properties," *JOM*, vol. 68, no. 3, pp. 1012–1020, Mar 2016.
- [22] A. S. Wu, D. W. Brown, M. Kumar, G. F. Gallegos, and W. E. King, "An experimental investigation into additive manufacturing-induced residual stresses in 316l stainless steel," *Metallurgical and Materials Transactions A*, vol. 45, no. 13, pp. 6260–6270, Dec 2014.
- [23] W. Devesse, D. De Baere, M. Hinderdael, and P. Guillaume, "Model-based temperature feedback control of laser cladding using high-resolution hyperspectral imaging," *IEEE/ASME Transactions on Mechatronics*, 2017.
- [24] R. Paul, S. Anand, and F. Gerner, "Effect of thermal deformation on part errors in metal powder based additive manufacturing processes," ASME. J. Manuf. Sci. Eng., vol. 136, no. 3, 2014.
- [25] C. Seidel, M. Zaeh, M. Wunderer, J. Weirather, T. Krol, and M. Ott, "Simulation of the laser beam melting process approaches for an efficient modelling of the beam-material interaction," *Procedia CIRP*, vol. 25, pp. 146 – 153, 2014, 8th International Conference on Digital Enterprise Technology - DET 2014 Disruptive Innovation in Manufacturing Engineering towards the 4th Industrial Revolution.
- [26] R. D. Cook, D. S. Malkus, and M. E. Plesha, Concepts and Applications of Finite Element Analysis, 3rd ed., R. D. Cook, D. S. Malkus, and M. E. Plesha, Eds. John Wiley and Sons, Inc., 1989.
- [27] R. D. Cook, D. S. Malkus, M. E. Plesha, and R. J. Witt, *Concepts and Applications of Finite Element Analysis*, 4th ed., W. Anderson, Ed. John Wiley and Sons, Inc., 2002.
- [28] C. R. Johnson, "The inertia of a product of two hermitian matrices," Journal of Mathematical Analysis and Applications, vol. 57, pp. 85– 90, 1977.
- [29] C.-T. Chen, Linear system theory and design, 3rd ed. New York, NY: Oxford University Press, 1999.
- [30] W. L. Brogan, Modern Control Theory. Prentice-Hall, 1985, ch. 11, pp. 376–377.
- [31] G. H. Golub and J. H. Wilkinson, "Ill-conditioned eigensystems and the computation of the jordan canonical form," SIAM Review, vol. 18, no. 4, pp. 578–619, 1976.
- [32] G. E. Dullerud and F. Paganini, A Course in Robust Control Theory. Springer, 2000.
- [33] L. Cao and H. M. Schwartz, "Analysis of the Kalman filter based estimation algorithm: an orthogonal decomposition approach," *Automatica*, vol. 40, p. 5 19, 2004.
- [34] K. Fathian, F. Hassanipour, and N. R. Gans, "Virtual thermal sensing and control of heat distribution using state estimation," in *Proceedings* of the ASME 2012 International Mechanical Engineering Congress & Exposition, Houston, TX, 2012, pp. 1725–1738.
- [35] K. Zeng, D. Pal, C. Teng, and B. E. Stucker, "Evaluations of effective thermal conductivity of support structures in selective laser melting," *Additive Manufacturing*, vol. 6, no. Supplement C, pp. 67 – 73, 2015.